Accepted Manuscript

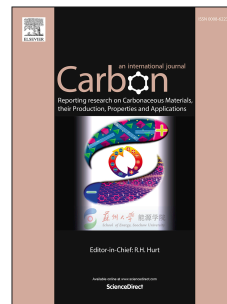

Influence of oxide substrates on monolayer graphene doping process by thermal treatments in oxygen

Angelo Armano, Gianpiero Buscarino, Marco Cannas, Franco Mario Gelardi, Filippo Giannazzo, Emanuela Schilirò, Raffaella Lo Nigro, Simonpietro Agnello

PII: S0008-6223(19)30399-9

DOI: https://doi.org/10.1016/j.carbon.2019.04.065

Reference: CARBON 14149

To appear in: *Carbon*

Received Date: 13 February 2019

Revised Date: 22 March 2019

Accepted Date: 16 April 2019

Please cite this article as: A. Armano, G. Buscarino, M. Cannas, F.M. Gelardi, F. Giannazzo, E. Schilirò, R. Lo Nigro, S. Agnello, Influence of oxide substrates on monolayer graphene doping process by thermal treatments in oxygen, *Carbon* (2019), doi: https://doi.org/10.1016/j.carbon.2019.04.065.

This is a PDF file of an unedited manuscript that has been accepted for publication. As a service to our customers we are providing this early version of the manuscript. The manuscript will undergo copyediting, typesetting, and review of the resulting proof before it is published in its final form. Please note that during the production process errors may be discovered which could affect the content, and all legal disclaimers that apply to the journal pertain.

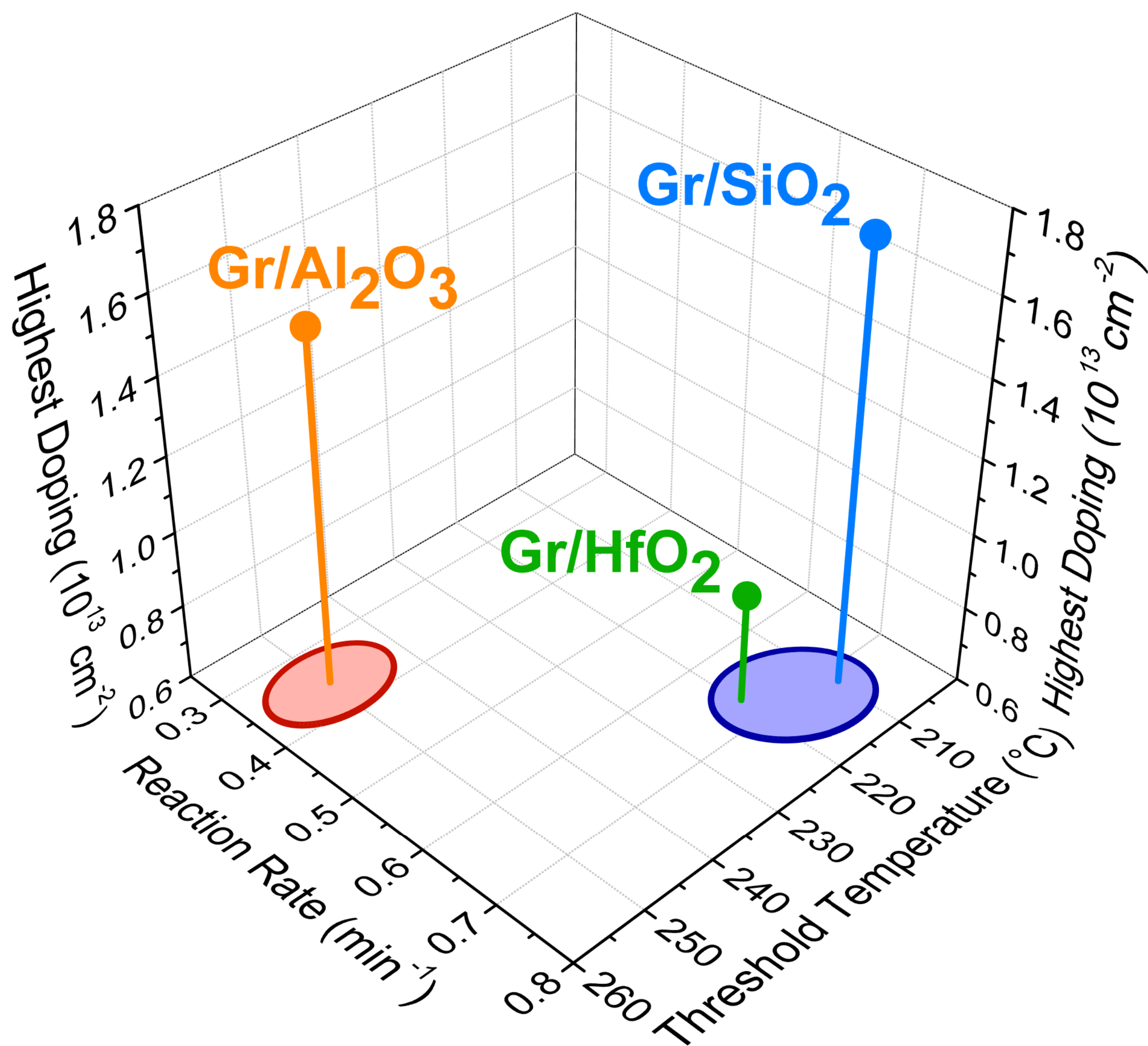

ACCEPTED

ACCEPTED MANUSCRIPT

Influence of oxide substrates on monolayer graphene doping process by thermal treatments in oxygen

Angelo Armano[a,b], Gianpiero Buscarino[a,c,d], Marco Cannas[a], Franco Mario Gelardi[a], Filippo Giannazzo[d], Emanuela Schilirò[d], Raffaella Lo Nigro[d], Simonpietro Agnello[a,c,d,*]

[a] *Università degli Studi di Palermo, Dipartimento di Fisica e Chimica - Emilio Segrè, Via Archirafi 36, 90123 Palermo, Italia*
[b] *Università degli Studi di Catania, Dipartimento di Fisica e Astronomia, Via Santa Sofia 64, 95123 Catania, Italia*
[c] *Università degli Studi di Palermo, ATeN Center, Viale delle Scienze, Edificio 18, 90128 Palermo, Italia*
[d] *Consiglio Nazionale delle Ricerche-Istituto per la Microelettronica e Microsistemi, Strada VIII 5, 95121 Catania, Italia*

Abstract

The structural and the electronic properties of monolayer graphene made by chemical vapor deposition and transferred on various oxide substrates (SiO_2, Al_2O_3, and HfO_2) are investigated by Raman Spectroscopy and Atomic Force Microscopy in order to highlight the influence of the substrate on the features of p-doping obtained by O_2 thermal treatments. By varing the treatment temperature up to 400 °C, the distribution of the reaction sites of the substrates is evaluated. Their total concentration and the consequent highest doping available is determined and it is shown that this latter is linked to the water affinity of the substrate. Finally, by varing the exposure time to the gas up to 2 hours, the kinetics of doping is investigated. The doping process is found to be better described by a diffusion limited kinetic model, ascribable to the diffusion of O_2 in the interstitial space between graphene and the

*Corresponding author
Email address: simonpietro.agnello@unipa.it (Simonpietro Agnello)

ACCEPTED MANUSCRIPT

substrate. After this step, the doping process is completed by a faster redox reaction between O_2 adsorbed to graphene and interstitial H_2O.

1. Introduction

Graphene is a carbon based nanomaterial which is composed by sp^2 hybridized carbon atoms only, and which can be considered as the basic component of graphite [1]. The peculiar two-dimensional structure provides graphene some excellent – and sometimes contradictory – properties, such as a high charge carrier mobility, high thermal conduction, good optical transparency, chemical stability, environment sensitivity, mechanical resistance, and flexibility [2–4]. These characteristics make graphene, and in particular graphene made by chemical vapor deposition [5, 6], very interesting for many applications in microelectronics such as field effect transistors, radiofrequency transistors, vertical THz transistors [7–9], volatile memories [10], composite nanomaterials [11–14] solar cells and rigid or flexible capacitive systems [2, 6, 15–17]. However, part of the operating capability of these graphene based devices resides in the introduction of high-k oxides in their design [18–20]. These materials were introduced to overcome tunneling effect between gate and substrate occurring by using nanoscale silica (SiO_2) as insulating layer [21, 22]. The typical values of k are comprised between 10 and 30, due to the limit imposed by the energy band gap of silicon [22, 23]. In particular, between the wide number of possibilities, alumina (Al_2O_3) with k=9, and hafnia (HfO_2) with k=25, are currently the most commonly chosen materials for this application [23, 24].

In this scenario, aiming to include graphene in the above reported applications, it is a basic requirement to achieve the fine engineering of its properties. In particular, to control the charge doping level provides the opportunity to

ACCEPTED MANUSCRIPT

25 tune the charge carrier concentration and charge sign of graphene, thus allowing to enhance its on plane conductivity and fabricate two-dimensional p-n junctions. To pursue this target, it is useful to employ the excellent sensitivity of graphene to environment. In fact, the adsorption of a large variety of chemicals on graphene interacts with the electron states and mod-
30 ifies its electric properties [3, 25]. Among the various available chemicals, our previous investigations have already shown that molecular oxygen is an easy and good choice to induce reversible p-type doping in Gr by means of thermal treatments in controlled atmosphere,while keeping undamaged the structure of Gr [26–29]. In literature, various processes are suggested to be
35 the cause of graphene doping by molecular oxygen: the reversible adsorption of oxygen molecules to the graphene basal plane [30–32], and a red-ox reaction between oxygen and water, catalyzed by graphene which provides the required electrons [33–35]. In any case, an electron transfer from graphene to the reactants has to occur, to justify the hole doping. The role of the
40 substrate in this kind of doping process for graphene is fundamental. In fact, as indicated by various investigations, the most relevant contribution to doping is attributed to the bottom face of graphene, thus suggesting that the substrate allows to stably preserve the reaction products which cause charge doping in graphene [36]. According to this hypothesis, the doping efficient
45 reaction sites must be ascribed not only to graphene but to the entire couple graphene-substrate, where for the latter, a fundamental role for the capability to doping is adduced. Therefore, the investigation of this doping process cannot prescind from the evaluation of the influence of different substrates, which has been shown to be relevant in other studies [37].

50 In this work, we report a study of the influence of different dielectric substrates (Al_2O_3 and HfO_2) on the doping process of graphene, by extending

the investigation formerly pursued for graphene on silica (SiO_2) substrate [29, 38–40]. In particular, the effect of the substrate on graphene is revealed by distinguishing the specific doping and strain configurations in the native samples and by investigating the different dependence of graphene doping on treatment parameters: temperature and exposure time. Thus, on varying the substrate, different temperature distributions of reaction sites for doping are revealed, as well as different time-scales of kynetics for doping occurrence and loss.

2. Materials and Methods

Commercial monolayer graphene (Gr) produced by Graphenea Inc. was used for the entire set of samples herein compared. Each sample is derived from the same batch. According to the manufacturing specifications, Gr was grown on Cu foil by chemical vapor deposition technique, at a temperature of 1000°C, using CH_4 as the carbon source. In order to transfer the Gr on the substrates, a layer of Poly(methyl methacrylate) (PMMA) was spin coated onto Gr/Cu, and then a thermal release tape (TRT) was laminated on PMMA. The Cu foil was etched by immersion in an ammonium persulfate water solution. The remaining TRT/PMMA/Gr stack was transferred to the various substrates by thermo-compression printing causing the release of TRT, and was cleaned from PMMA layer by an acetone bath. We employed two silicon substrates coated by ∼40 nm of Al_2O_3 and ∼50 nm of HfO_2, respectively. The Al_2O_3 thin film was grown by thermal atomic layer deposition (ALD) at 250°C, using tri-methyl aluminum (TMA) and H_2O as the aluminum and oxygen precursors, respectively. HfO_2 was deposited by plasma enhanced ALD at 250°C, using tetrakis-dimethylamino hafnium (TDMA-Hf) as the hafnium precursor and O_2-plasma as oxygen

ACCEPTED MANUSCRIPT

source. In addition, a substrate with a 300 nm SiO_2 was used for comparison. For simplicity's sake, these samples are labeled in this work as Gr/Al_2O_3 and Gr/HfO_2, and Gr/SiO_2. For the latter sample, the reference data are reported from Refs. [29, 38, 39] for the same Gr.

The thermal treatments of the samples were performed by an apparatus comprising a stainless steel chamber of about 100 mL volume with controllable temperature and pressure. For each treatment, after a pre-vacuum at pressure of 0.3 mbar, nitrogen (TTN_2) or oxygen (TTO_2) gases at pressure of 2 bar with 20 ppm mol of impurities were used for selective experiments. Treatment temperature and total time were varied in the range 150–400 ℃, and 5–125 minutes, respectively. For *direct* treatments (with reference to previous investigations), a temperature of 300 ℃ and an exposure time of 2 hours were used.

Raman Spectroscopy was performed using a Bruker SENTERRA μ-Raman spectrometer equipped with a confocal optical microscopy system with 50× optical magnification; a best spectral resolution equal to 9 cm^{-1}, and a data pitch equal to 0.5 cm^{-1} were employed. All the measurements were performed with a 532 nm (2.33 eV) excitation laser at nominal power equal to 5 mW. All the spectra were aligned to the silicon band located at 520.7 cm^{-1} [41, 42]. Since the Raman signal amplitude of Gr heavily depends on the optical properties (such as thickness and refractive index) [43], different target areas were used to collect the Raman signal. In particular, a target area of 4×4 μm^2 for Gr/Al_2O_3, and a larger area equal to 4×15 μm^2 for Gr/HfO_2. For each sample, a set of more than 20 measurements was acquired in order to evaluate heterogeneity and to determine the mean values for the Gr spectroscopic features. Therefore, each spectrum yields the following quantities: G and 2D band peak position ($\bar{\nu}_G$ and $\bar{\nu}_{2D}$), their full width at half maximum (FWHM)

105 (Γ_G and Γ_{2D}) and the ratio of their peak amplitude ($I(\bar{\nu}_{2D})/I(\bar{\nu}_G) = R$) [44]. The uncertainty of the reported values is expressed in terms of one standard deviation of each values distribution in parenthesis. By means of a ($\bar{\nu}_G$, $\bar{\nu}_{2D}$) map, the correlation analysis of G and 2D peak positions was used to evaluate the structural and electronic deviation of Gr from its ideal features (namely 110 doping and strain occurrence) [45]. In particular, for the calculation of doping, the same approximated relation of Ref. [46] has been used. Besides, for the calculation of strain, the dispersion relation that binds volume and mode frequencies, and a Grüneisen parameter for graphene equal to 3.55 have been used [47–49]. In the G-2D correlation map reported in the following, ac- 115 cording to the excitation energy of 2.33 eV, two dotted lines whose slopes are equal to 2.45 and 0.7, respectively, mark the couples of values ($\bar{\nu}_G$,$\bar{\nu}_{2D}$) which are equivalent to only strain or p-type doping effects [39, 46]. Other positions in the graph are interpreted in terms of the vectorial compositions of concurrent doping (D) and strain (ϵ) effects whose single evaluation is 120 achieved by the projection of each point on the respective axes [47–49].

Atomic Force Microscopy (AFM) measurements were performed in Tapping Mode by using a Bruker FastScan Bio and Bruker FastScan A probes with tip radius approximately equal to 5 nm. AFM images were acquired on different micrometric scales, up to 5×5 μm^2 of area. Information of 125 quantitative nature was extracted by means of Gwyddion v. 2.52 software (`http://gwyddion.net`).

The static contact angles (CA) have been measured using a Smart CAM 200 goniometer. The system mainly consists of a syringe for accurately control the volume of the deposited drop and of a CCD camera, with a resolution 130 of 512×480 pixels. The drop image, stored by the video camera with subpixel accuracy, is fitted to the Young-Laplace equation in order to calculate

the left and right angles with an accuracy of $\pm 0.1^\circ$. For these measurements, a droplet size of 3 μL ($\sim$2 mm of diameter) of water has been used. The contact angle of the samples was measured at four different places on the
135 substrate. Herein, we report the average value and the standard deviation as uncertainty estimation.

3. Results and Discussion

3.1. Substrates

The preliminary characterization of the used substrates is given in terms
140 of the morphological and chemical properties which can influence the Gr structural and electronic features. The surface morphology of graphene-free substrates was evaluated from the AFM images reported in Figure S1. By taking care to discard the clusters of residual PMMA, we obtained a value of roughness equal to 0.22(1) nm for SiO_2, 0.31(1) nm for Al_2O_3, and 0.13(2) nm
145 for HfO_2, respectively. In addition, the water affinity of the substrates was evaluated in terms of CA, which resulted equal to $60(2)^\circ$ for SiO_2, $74(1)^\circ$ for Al_2O_3, and $87(2)^\circ$ for HfO_2, respectively. By convention, since these values are lower than 90°, the surface of each sample has to be considered hydrophilic, but a different degree of water affinity is revealed.

150 ### *3.2. Native samples*

The typical native Gr/HfO_2 and Gr/Al_2O_3 Raman spectra are compared in Figure 1 to a reference spectrum of native Gr/SiO_2, reported in Ref. [38]. The strong influence of the oxide thickness and dielectric constant on the signal intensity of Gr reported in literature [43] justifies the different sig-
155 nal/noise ratio observed in the spectral region between 1200 and 1700 cm^{-1} on varying the substrate. Every spectra clearly show the G and the 2D

ACCEPTED MANUSCRIPT

bands, characteristic of graphene. Because the ratio R is higher than 1, we can confirm the monolayer nature of transferred Gr. Moreover, the low intensity of D band – located at ∼1340 cm^{-1} – allows us to state that the number
160 of carbon atoms in sp^2 hybridization prevails on the contribution of defects concentration.

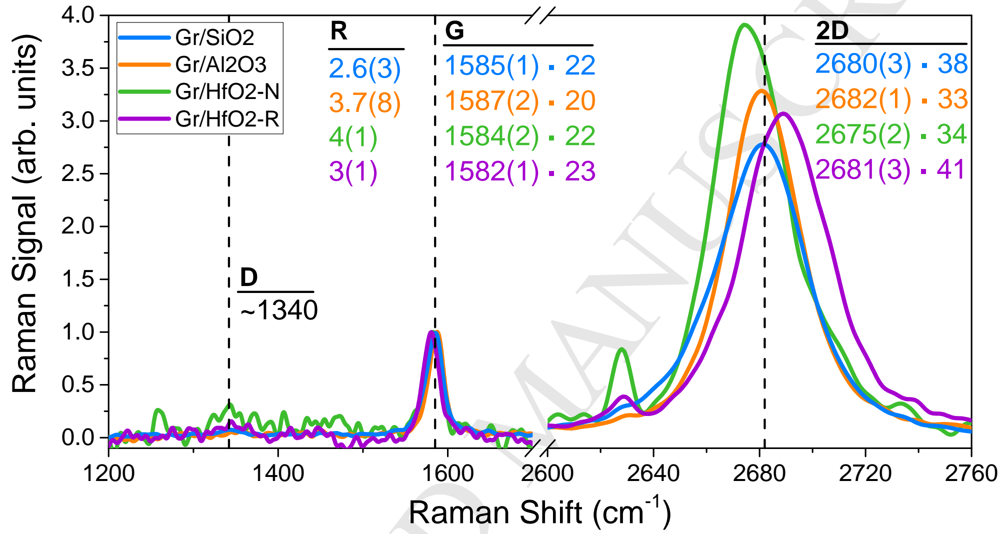

Figure 1: Raman spectra normalized at G peak amplitude of Gr/SiO_2 (azure) from Ref. [38], Gr/Al_2O_3 (orange), Gr/HfO_2-N (green) and Gr/HfO_2-R (violet). Dashed lines mark the peak position of D, G, and 2D bands for Gr/SiO_2 sample. For each sample, amplitude ratio R, peak positions $\bar{\nu}$ and FWHM Γ are reported. The uncertainty value for the last digit is reported in parenthesis.

For Gr/SiO_2 sample, the reference data report $\bar{\nu}_G$=1585(1) cm^{-1}, $\bar{\nu}_{2D}$=2680(3) cm^{-1}, Γ_G=22(3) cm^{-1}, Γ_{2D}=38(3) cm^{-1} and R=2.6(3) [38] and for Gr/Al_2O_3 sample, we determined $\bar{\nu}_G$=1587(2) cm^{-1}, $\bar{\nu}_{2D}$=2682(1) cm^{-1}, Γ_G=20(3) cm^{-1},
165 Γ_{2D}=33(2) cm^{-1} and R=3.7(8). On the other and, for Gr/HfO_2 samples, as will be clarified in the following, two distinct configurations are revealed. The first one, named Gr/HfO_2-N, has mean values $\bar{\nu}_G$=1584(2) cm^{-1}, $\bar{\nu}_{2D}$=2675(2) cm^{-1},

ACCEPTED MANUSCRIPT

Γ_G=22(3) cm^{-1}, Γ_{2D}=34(5) cm^{-1} and R=4(1); the second one, named Gr/HfO_2-R, has mean values $\bar{\nu}_G$=1582(1) cm^{-1}, $\bar{\nu}_{2D}$=2681(3) cm^{-1}, Γ_G=23(2) cm^{-1},
170 Γ_{2D}=41(5) cm^{-1} and R=3(1).

The study of correlation between G and 2D peak positions, reported in Figure 2, allowed to distinguish the three samples, which yield four different point clouds. Similarly to what was observed for Gr/SiO_2 (azure ellipse), Gr/Al_2O_3 (orange ellipse) constitutes a single point cloud which describes a
175 single mean configuration with its own spread on strain and doping values. On the contrary, in the case of Gr/HfO_2 we can recognize both a main cluster of points (green ellipse), and a minority group of points characterized by higher 2D frequency. In literature, this feature (and in general the spread

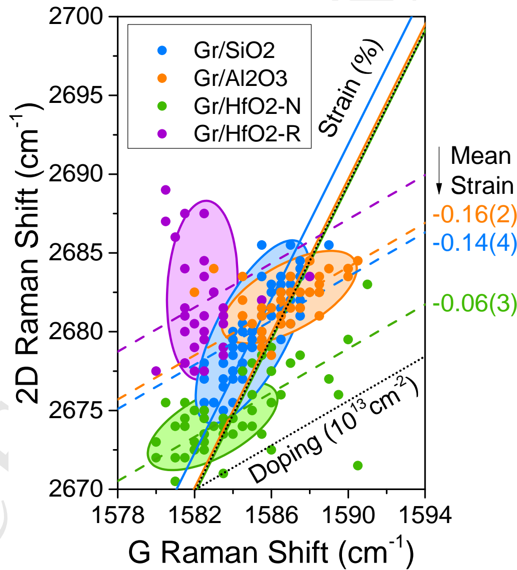

Figure 2: Correlation map between G and 2D peak position of Gr/SiO_2 (azure) from Ref. [38], Gr/Al_2O_3 (orange), Gr/HfO_2-N (green) and Gr/HfO_2-R (violet). Qualitative ellipses highlight the four point clouds. Dotted lines mark strain and doping axes. For each cloud, dashed lines and continuous lines mark the average strain and doping, respectively. The extracted values of strain are also reported. The uncertainty value for their last digit is reported in parenthesis.

ACCEPTED MANUSCRIPT

of measurements far left of the strain axis) is related to the reduction of the
180 Fermi velocity v_F in Gr [50, 51]. In particular, some works relate this reduction to a dielectric screening exerted by the substrate that can be found in case of high (as for HfO_2) or infinite (metals) k substrate and it is favored by a strong graphene-substrate coupling [51, 52]. On the contrary, other works relate the reduction to the presence of folded Gr in a non-AB stacking [53].
185 As reported in Figure S2, some regions of folded Gr were actually revealed in Gr/HfO_2, and because of the use of a larger acquisition area for Raman measurements, the involvement of these regions cannot be avoided. However, further effects due to the high-k substrate cannot be excluded by principle. Hereafter, we name Gr/HfO_2-N (normal) the cluster that does not show a
190 significant deviation at the left of strain axis, and Gr/HfO_2-R (reduced) the cluster featured by the reduction of v_F. The presence of this second species is not revealed in the other cases (except for few points in Gr/Al_2O_3), thus suggesting a peculiar interaction between graphene and some regions of HfO_2 substrate.

195 It is easy to notice that both Gr/Al_2O_3 and Gr/HfO_2-N point clouds show different *orientations* on G-2D map compared to Gr/SiO_2, thus suggesting a different heterogeneity in strain and doping configurations. In particular, their point clouds show a narrower distribution along the strain axis, and a broader distribution along the doping axis, indicating a more ordered struc-
200 ture, and a more heterogeneous electronic structure. For both samples, the doping value results below the minimum level of sensitivity of this technique, equal to 10^{12} cm^{-2} charge carriers concentration, and thus, in this case, a quantitative estimation is possible only for strain. As highlighted in Figure 2 by dashed lines, Gr/Al_2O_3 and Gr/HfO_2-N reach a mean strain equal to
205 ϵ=-0.16(2)% and ϵ=-0.06(3)%, respectively higher and lower than Gr/SiO_2,

which has a mean strain equal to ϵ=-0.14(4)% [38]. Concerning Gr/HfO_2-R, because of the additional shift due to the v_F reduction, the coarse projection to the strain axis will yield an incorrect evaluation. Herein, we assume that, if the Gr/HfO_2-R cluster had no v_F reduction, it would be placed in the same
210 position of Gr/HfO_2-N cluster with the same strain and doping features. By this assumption we assign the same value of strain ϵ=-0.06(3)% extracted for Gr/HfO_2-N and we estimate the reduction of Fermi velocity Δv_F=-3% for Gr/HfO_2-R [51, 53]. Since previous investigations have already shown

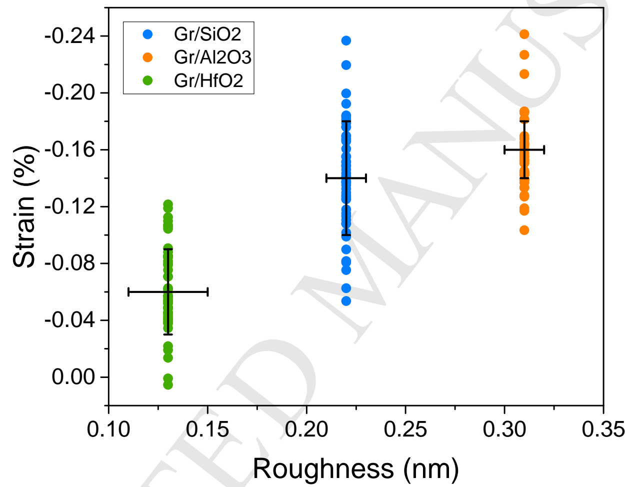

Figure 3: Correlation between Gr strain, evaluated by means of G-2D correlation analysis, and the substrate roughness evaluated by AFM, for Gr/SiO_2 (azure), Gr/Al_2O_3 (orange), Gr/HfO_2-N (green). The values of strain are extracted from Figure 2. The uncertainty values are reported as error bars around the strain and roughness mean value.

the close connection between Gr strain and its own roughness and that of
215 the substrate [38], the value of native Gr strain reported can be related to the different substrate morphology. Based on these findings the correlation between the Gr strain and the substrate roughness was evaluated, revealing a relation of proportionality between them, as shown in Figure 3, thus indicating that some structural features of native Gr depend on how the Gr lies

ACCEPTED MANUSCRIPT

220 down on the substrate after the transfer process. Nevertheless, it is known that the native configuration is not fixed, but can be modified by opportune thermal treatments [38].

3.3. Atmosphere Effect

In order to discern the doping effect of O_2 from the pure thermal effect, we compare the results of thermal treatments in O_2, and in N_2, namely reactive and inert atmosphere, respectively, basing also on previous experiments carried on SiO_2 substrate [39]. The typical spectra of thermally treated Gr/Al_2O_3, Gr/HfO_2-N, and Gr/HfO_2-R are reported in Figure 4a,b and compared with the spectra of the respective native samples of Figure 1. As reported in Figure 4a,b, (as well as in Figure S3a,b for a wide set of measurements), the thermal treatment in O_2 modifies heavily the ratio R, by drasticly reducing it, similar to the case of Gr/SiO_2 [38, 39]. In both cases, G and 2D peak positions blueshift, and moreover, G and 2D FWHMs are modified (Figure S3c,d), with a greater contribution for O_2 treatment. Similar to the case of Gr/SiO_2, Gr/Al_2O_3 shows no modification for the D band, confirming that the thermal treatment preserves the *sp*^{2} structure of graphene. Concerning the Gr/HfO_2, the low signal-noise ratio does not allow to detect the D band, and this makes it difficult to draw the same conclusion. However, a large occurrence of defect sites can be excluded by the peak amplitude ratio I_D/I_G which, even if hard to estimate, is certainly lower than 0.3 [44].

More information can be extracted from the analysis of the correlation between G and 2D peak positions. In the case of Gr/Al_2O_3, as shown in Figure 5a, the point clouds of both thermally treated samples are clearly shifted compared to the native one and similarly *dense*. On the contrary, in the case of Gr/HfO_2 (Figure 5b), the same thermal treatments in N_2 and O_2 atmospheres cause more heterogeneous results. In fact, even if a similar trend

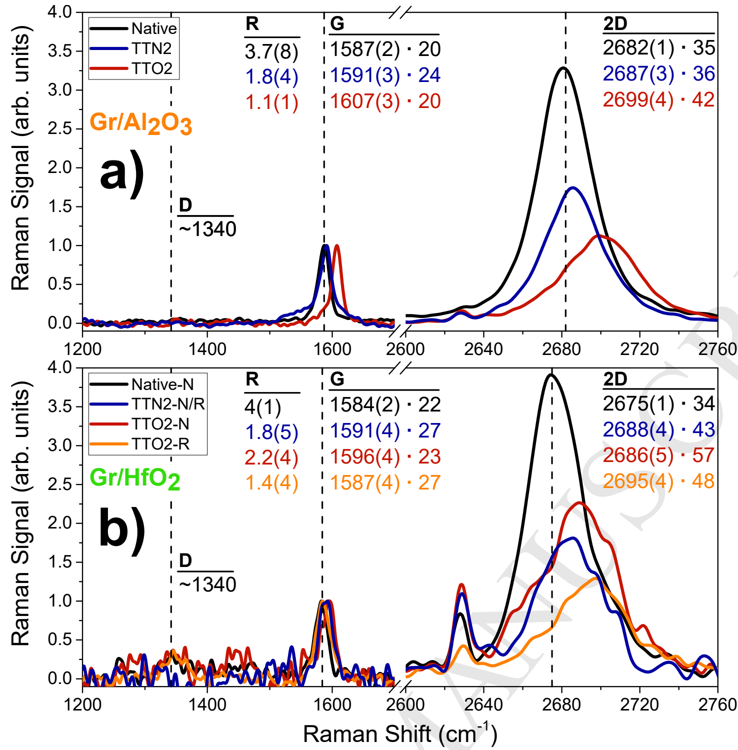

Figure 4: Raman spectra normalized at G peak amplitude of native (black), thermally treated samples in oxygen (red, TTO_2), and nitrogen (blue, TTN_2) atmosphere for **(a)** Gr/Al_2O_3 and **(b)** Gr/HfO_2. In the latter case, the results of the normal (red) and reduced (orange) species are distinguished. Dashed lines mark the peak position of D, G, and 2D bands for respective native samples. For every sample, bands ratio R, peak positions $\bar{\nu}$ and FWHM Γ are reported. The uncertainty value for the last digit is reported in parenthesis.

in the shifts is recognizable, both the point clouds appear largely spread on the graph, indicating a non-homogeneous effect of both strain and doping.

For N_2 treatment, the shape of point clouds is approximately similar to the native ones. In particular, for Gr/Al_2O_3, we observe an increase of spread along the doping axis with a slight increase of doping (at the limit of the sensitivity of this technique), reaching the values of D=0.2(2)$\times10^{13}$cm^{-2} and an increase of compressive strain up to ϵ=-0.21(3)%, the latter being similar to the case of Gr/SiO_2 [38]. Despite of the larger spread of point cloud, similar

255 mean values are obtained for Gr/HfO_2 for which we find: D=0.1(4)×10^{13}cm^{-2} and ϵ=-0.22(7)%. Because of the large spread of its point cloud and because

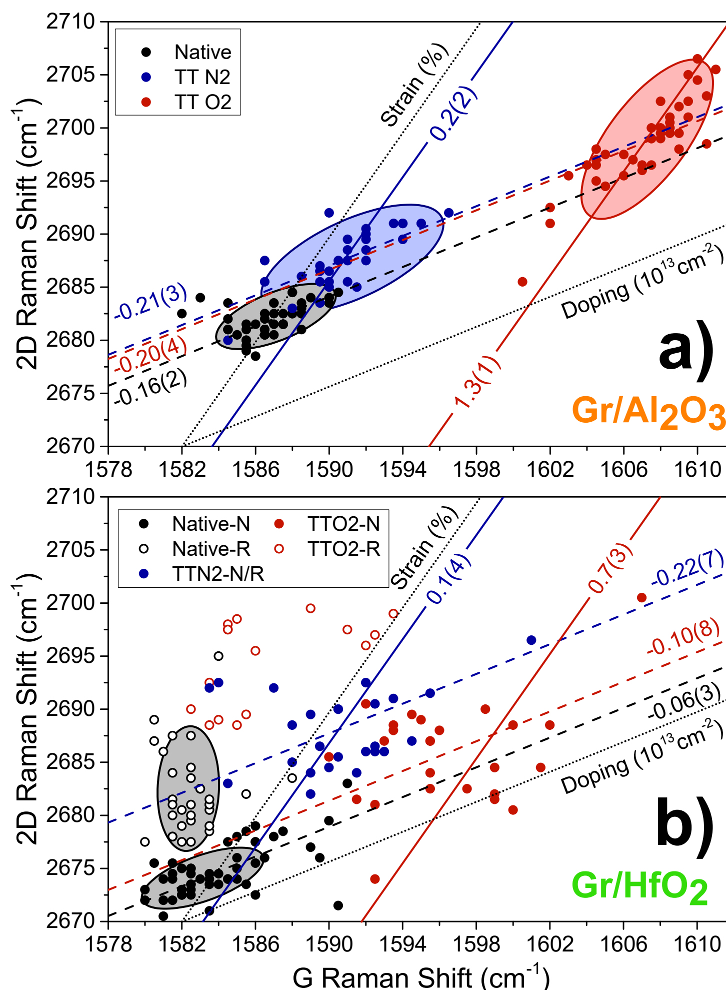

Figure 5: Correlation map between G and 2D peak position of native (black), and treated samples at T=300 °C, for 2 hours, at pressure of 2 bar of oxygen (red, TTO_2) and nitrogen (blue, TTN_2) atmosphere for **(a)** Gr/Al_2O_3 and **(b)** Gr/HfO_2. In the latter case, normal (filled circles) and reduced (empty circles) samples are distinguished. Qualitative ellipses highlight the dense point clouds. Dotted lines mark strain and doping axes. For each sample, dashed lines and continuous lines mark the average strain and doping, respectively. The extracted values of strain are also reported. The uncertainty value for their last digit is reported in parenthesis.

some points are located in the *forbidden zone* [54], far left of the strain axis (for which a reduction of Fermi velocity cannot be excluded), we assume that both kinds of native Gr/HfO_2 evolved with a similar increase of strain.

260 More considerable change occurs by the O_2 treatment, as reported in Figure 5. Concerning Gr/Al_2O_3, the point cloud is uniformly shifted to values of remarkable doping equal to D=1.3(1)×10^{13}cm^{-2}, contrary to previous investigations [39]. We can also notice that, compared to the native cloud, O_2 treated sample is affected by a larger spread along strain axis than along 265 doping axis, as well as a higher Γ_{2D} (Figure S3), suggesting that O_2 doping process involves the modification of the Gr structure to a more disordered configuration, more similar to typical native Gr/SiO_2. Moreover, we suggest that the decrease in doping spread and Γ_G is due to the doping process itself, which constrains the charge carrier concentration to a specific level, more 270 strictly determined than for the native (unintentional) doping. On the other hand, for Gr/HfO_2, the cloud features a very large spread, which we relate to strong structural and electronic heterogeneity. Similar to what done with the native sample, we discriminate the measurement set in two groups roughly separated by the strain axis: the group placed in the *forbidden zone* at the 275 left of the strain axis, and the group placed in the *doping zone* at the right of the strain axis. Because of its peculiar location, no quantitative estimation of doping can be done for group to the left. In order to try to evaluate where this group would be placed if it had no reduction of Fermi velocity, we shift it vertically (only along 2D axis) and we find that only zone at low 280 doping values is involved. Therefore, no doping process affects the group at the left of the strain axis, and we conclude that this group results only by the evolution of the native Gr/HfO_2-R, whereas the group placed in the *doping zone* results only by the evolution of the native Gr/HfO_2-N point cloud. As a

consequence, the reduction of Fermi velocity and the capability to doping re-
285 sult to be mutually exclusive for native Gr/HfO_2. Thus, by considering only the group at the right of the strain axis, we estimate a doping level equal to D=0.7(3)$\times 10^{13}$cm^{-2}, on average lower than in the case of Gr/SiO_2 [38].

Finally, concerning the strain, Gr/Al_2O_3 reaches the value of ϵ=-0.20(4)% (comparable to N_2 treatments), whereas Gr/HfO_2 reaches the value ϵ=-0.10(8)%
290 (lower than N_2 treatments), a feature different and similar, respectively, to the case of Gr/SiO_2 [38]. These results clearly show the close dependence of the structural and electronic evolution of graphene by thermal treatments on the underlying substrate.

3.4. Doping vs Temperature

295 The dependence on temperature of doping induced by O_2 has been investigated by performing, on the same sample, a series of thermal treatments, with duration of 2 hours each and increasing the temperature by steps of 25 ℃ up to 400 ℃ and evaluating *ex-situ* the doping occurrence.

As shown in Figure 6, a progressive increase in the doping is revealed
300 for both Gr/Al_2O_3 and Gr/HfO_2-N, also traceable by the decrease of the ratio R (reported in Figure S4), whereas no doping is induced for Gr/HfO_2-R. Concerning the strain, a slight increase of compressive strain is revealed for GrAl_2O_3 and Gr/HfO_2-N, contrary to what is reported for Gr/SiO_2 [29] where a strong decrease of strain was revealed at maximum doping levels
305 (Figure S5). Nevertheless, both Gr/HfO_2-R and Gr/HfO_2-N points with low doping evidence higher strain compared to native samples, similarly to Gr/SiO_2 in analogous doping state [38]. It is important to note that, as revealed in the previous section, a broadening of strain values distribution occurs on the increase of doping for Gr/Al_2O_3 and Gr/HfO_2-N. Through the
310 regulated increase of doping by temperature, we can reveal the progressive

ACCEPTED MANUSCRIPT

evolution of strain spread, and most importantly, the heterogeneity which characterizes this change. In fact, as reported in Figure S4, the increase of Γ_{2D} against $\bar{\nu}_G$ (that approximately means against doping) indicates an increase of structural disorder, strengthening the idea of a correlation between

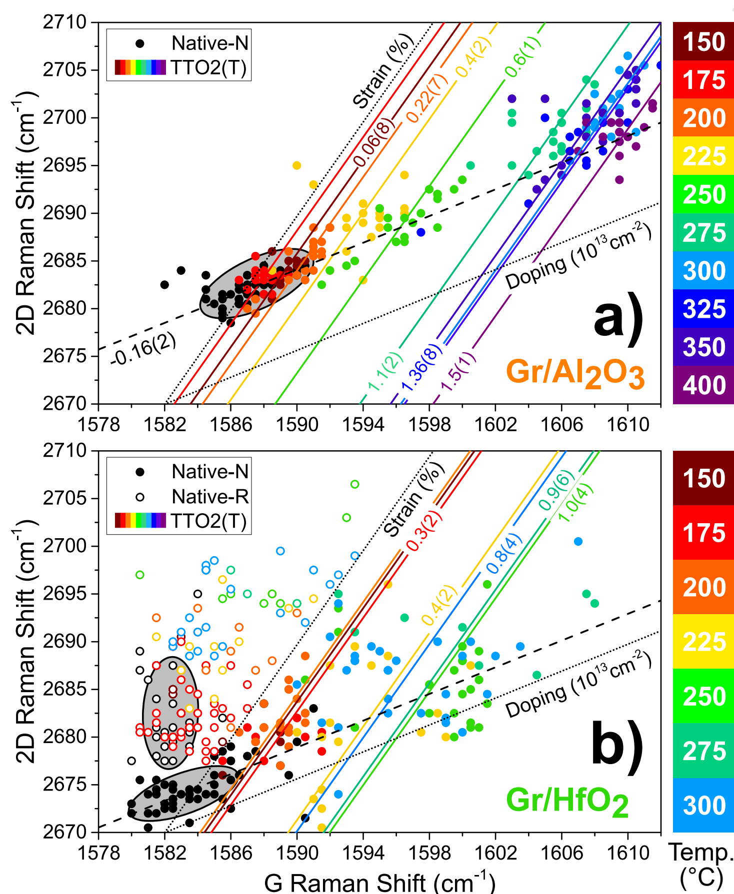

Figure 6: Correlation map between G and 2D peak position of native (black), and thermally treated samples in oxygen (TTO_2) atmosphere on increasing of temperature (color scale) of **(a)** Gr/Al_2O_3 and **(b)** Gr/HfO_2. In this latter case, both normal (N) and reduced (R) kinds of Gr are shown by filled and empty circles, respectively. Dotted lines represent the reference strain and doping axes. Dashed lines and continuous lines mark the average strain and doping, respectively. The extracted values are also reported. The uncertainty value for their last digit is reported in parenthesis.

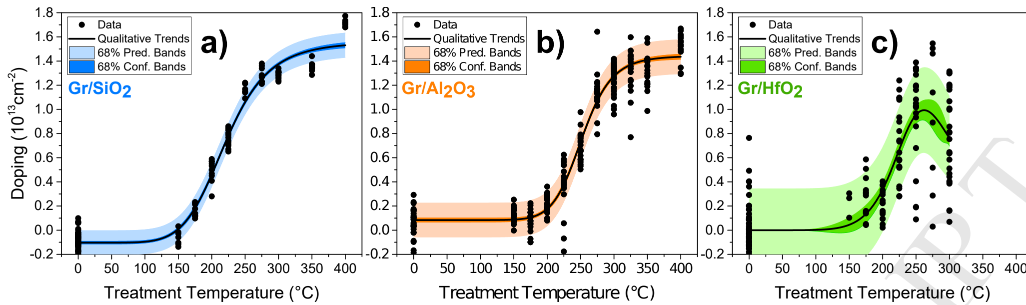

Figure 7: Extracted doping values on varying temperature for **(a)** Gr/SiO_2, **(b)** Gr/Al_2O_3, and **(c)** Gr/HfO_2. Qualitative trends are reported. Their uncertainty is reported by the prediction and confidence bands at one standard deviation by the Logistic and BiHill curves provided by Origin (OriginLab, Northampton, MA) function library.

315 doping process and structural reassessment of Gr structure. Most importantly, Γ_{2D} reaches a peak value at intermediate temperature, indicating a range of higher structural disorder for intermediate doping. Such a evolution does not occur in Gr/SiO_2, which keeps the same strain spread and Γ_{2D} even at intermediate doping.

320 The estimation of doping levels, extracted from the position of each measurement, is reported in Figure 7 (data for Gr/SiO_2 are reported from Ref. [29]). For all samples, the doping increases with the temperature through a sigmoidal trend, featured by a threshold temperature followed by the approach to a maximum level. This sigmoidal trend is more evident in Gr/SiO_2 325 and Gr/Al_2O_3 (Figure 7a,b) than in Gr/HfO_2 (Figure 7c), because of the larger spread of values of the latter sample. The comparison of the three general trends, simplifies the recognition of different features: a lower threshold for both Gr/SiO_2 and Gr/HfO_2 compared to Gr/Al_2O_3, and the decrease of doping at temperature higher than 250 ℃ for Gr/HfO_2 which reaches an over- 330 all lower doping level. Because temperature higher than 400 ℃ causes the destruction of Gr for Gr/SiO_2 and Gr/Al_2O_3 samples, that temperature de-

ACCEPTED MANUSCRIPT

termines the highest doping available, which is equal to $1.75(9)\times10^{13}$cm^{-2} and $1.54(9)\times10^{13}$cm^{-2}, respectively. On the other hand, in the case of Gr/HfO_2, because at temperature higher than 250°C an additional trend of doping de-
335 crease is noticeable, the highest doping available is determined at this limit temperature, and equal to $0.9(4)\times10^{13}$cm^{-2}. The highest doping reached can also be expressed in terms of number of charge carriers per unit of C atoms as equal to 0.45(3)%, 0.39(3)%, and 0.24(9)% for Gr/SiO_2, Gr/Al_2O_3 and Gr/HfO_2, respectively.

340 Because of the fundamental role of the substrate for the doping process (already cited in the introduction), it is legitimate to ascribe the different behaviors here reported to the different used substrates. Therefore, by considering also the heterogeneity of doping related structural changes indicated by the evolution of Γ_{2D}, we propose a model where these three curves are
345 interpreted as the cumulative contribution to doping provided by the fraction of the reaction sites whose activation temperature is below to the treatment temperature. Thus, for each system, we can obtain the distribution in temperature of the reaction sites N_{RS} by the derivative against temperature of doping trend curve: $N_{RS}(T) \propto \partial D/\partial T$.

350 The obtainted distributions, reported in Figure 8, are featured by the mean position which marks the maximum population, and the FWHM which describes the range of temperature which provides doping occurrence: (210±50)°C, (250±40)°C, and (220±30)°C for Gr/SiO_2, Gr/Al_2O_3, and Gr/HfO_2, respectively. In particular, the doping occurrence is represented by positive sign
355 population, and linked to the activation of an ever large fraction of reaction sites of the Gr-substrate system on increasing of temperature, whereas the doping loss observed for Gr/HfO_2 is represented by negative sign population. As depicted in Figure 9, according to the proposed model, all the reaction

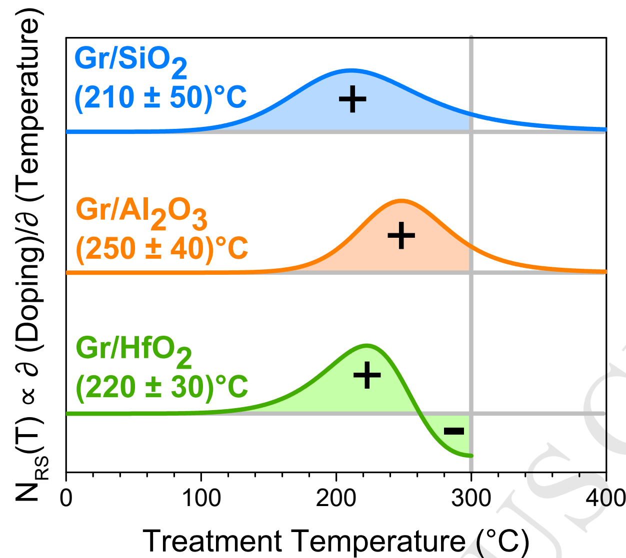

Figure 8: Comparison of the reaction sites distribution N_{RS} for Gr/SiO_2(azure), Gr/Al_2O_3 (orange), and Gr/HfO_2 (green). Positive (+) or negative (–) contribution to doping is highlighted. On a given temperature (for example, 300°C) all the sites activated at lower temperature (colored areas) contribute to the final doping value.

sites activated below a given temperature contribute to the doping process (blue diamond), whereas the remaining sites keep unreacted (red crosses). Furthermore, the approach to the saturation value may be ascribable to the exhaustion of the reaction sites, which continuously reduces the contribution of further reactions. The different maximum doping available, is thus related to the integral of the N_{RS} distribution, that is the different density of reaction sites for the three substrates.

Finally, we compare the highest doping level with the water affinity of the various substrate surfaces, the latter being evaluated in terms of contact angle measured before the Gr transfer. As reported in Figure 10, the doping capability is favored by the substrate hydrophilicity that, for the considered oxides, is typically related to the presence of hydroxil groups on the surface [55–58]. By considering the oxygen reduction reaction suggested in

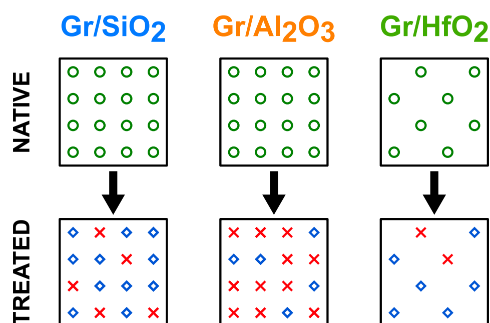

Figure 9: Graphical representation of the proposed model for the doping reaction. For the the native samples (top line), the different substrates are distinguished by their peculiar density of reactive sites (green circles). In bottom line, as effect of the thermal treatment at a given temperature, because of their temperature distribution shown in Figure 7, only a fraction of sites reacts with the O_2 (blue diamonds), whereas some sites remain inactive (red crosses).

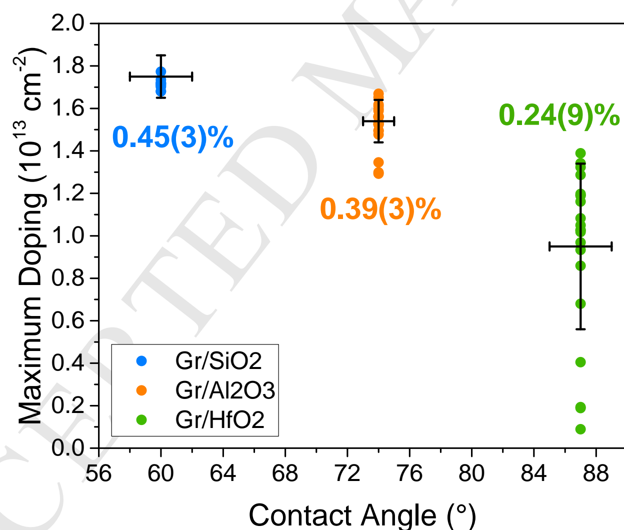

Figure 10: Dependence of maximum available doping on the degree of hydrophilicity of the substrate, as measured by wetting contact angle before the transfer of Gr. Mean values and their uncertainty are reported by error bars. For each sample, the percentage of doped C atoms is also reported. Data at temperature equal to 400 °C for Gr/SiO_2, Gr/Al_2O_3, and 250 °C for Gr/HfO_2 have been used.

ACCEPTED MANUSCRIPT

literature, the two half-reaction involving the doping process are

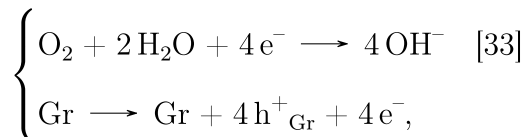

$$\begin{cases} O_2 + 2\,H_2O + 4\,e^- \longrightarrow 4\,OH^- \quad [33] \\ Gr \longrightarrow Gr + 4\,{h^+}_{Gr} + 4\,e^-, \end{cases}$$

where, contextually to the oxygen reduction, the Gr is oxidized, and therefore, doped by holes which result in its band occupation. For such a mechanism, the hydratation of the substrate surface is clearly mandatory in order to provide the necessary amount of water. The lower water affinity estimated for Gr/HfO_2 and Gr/Al_2O_3 compared to Gr/SiO_2, is fully compatible with their lower doping capability. Therefore, in accordance to the proposed model, the value of the highest doping level is a peculiar feature of each substrate related to its water affinity, and somehow, assumed to be proportional to the total number of the reacted sites depicted in Figure 9.

3.5. Doping vs Time

The kinetics of O_2 doping process was investigated in the range 5–125 minutes by performing successive thermal treatments at 300 ℃ (reference temperature for previous investigations), and evaluating *ex-situ* the doping as a function of total treatment time. As shown in Figure 11, the doping progressively increases with time up to a maximum value, the latter, by taking in account the previous discussion, is merely determined by the temperature. Moreover, as reported in Figure S6, the same spectroscopic evolutions of R and Γ_{2D} due to doping revealed with temperature increase are here confirmed. However, the fast doping occurrence prevents to finely observe the structural disorder occurring at intermediate doping. On the other hand, as shown in Figure S7, no clear trends are revealed for strain.

By extracting the doping levels from each measurement at various times, the different time-scales of doping are revealed, as reported in Figure 12,

ACCEPTED MANUSCRIPT

allowing to evidence the dependence of kinetics on the used substrate. In
390 particular, for Gr/SiO_2 (Figure 12a), which data are reported from [38], and for Gr/Al_2O_3 (Figure 12b) the doping monotonically increases with the

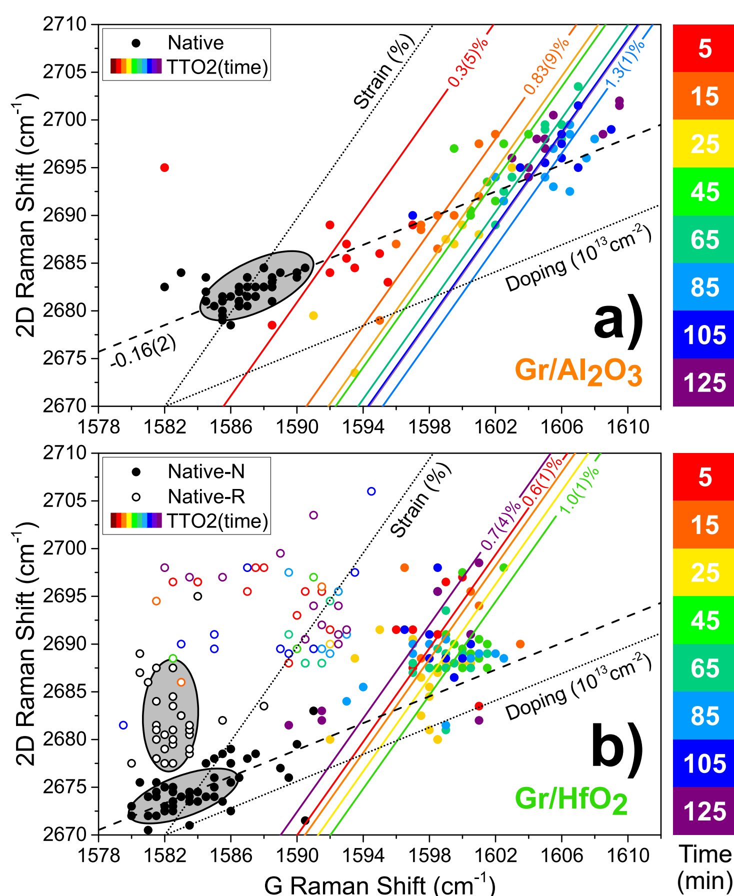

Figure 11: Correlation map between G and 2D peak position of native (black) thermally treated samples in oxygen (TTO_2) atmosphere on increase of treatment time (color scale) of **(a)** Gr/Al_2O_3 and **(b)** Gr/HfO_2. In this latter case, both normal (N) and reduced (R) kinds of Gr are shown by filled and empty circles, respectively. Dashed lines and continous lines mark the average strain and doping, respectively. The extracted values are also reported. The uncertainty value for their last digit is reported in parenthesis.

time up to reach a saturation level. On the contrary, in the case of Gr/HfO_2 (Figure 12c), after a fast initial increase, the progressive loss of doping is

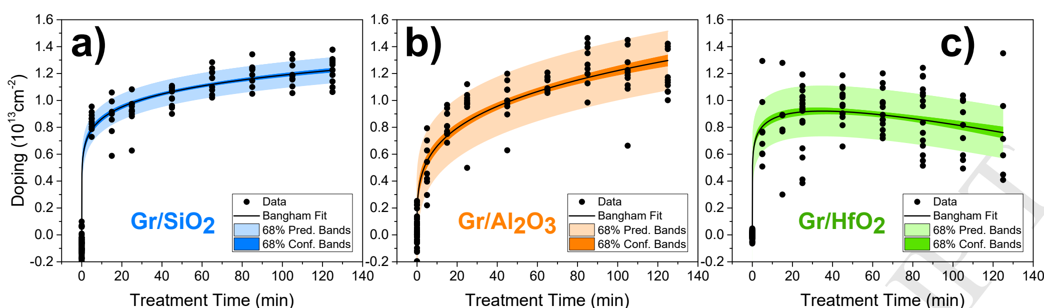

Figure 12: Extracted doping values on increasing treatment time for **(a)** Gr/SiO_2, **(b)** Gr/Al_2O_3, and **(c)** Gr/HfO_2. The kinetics of doping occurrence is reported by the Bangham model, which best fitted the data. Fit uncertainty is reported by the prediction and confidence bands at one standard deviation by the best fit curve. A modified version of Bangham model was used for Gr/HfO_2, in order to describe the loss of doping revealed for long time.

clearly revealed for time higher than 45 minutes. In fact, as reported in the
395 previous section, at the temperature used for the kinetics study, the doping removal process is also active.

In general, the adsorption based processes are usually composed by multiple steps dynamics, which include the diffusion of the reagents to the adsorption sites, followed by the actual adsorption, and the observed kinetics
400 is determined by the step which occurs more slowly [59–62]. Therefore, both diffusional and adsorption models are taken into account so as to discriminate if the time scale of doping occurrence is rate-limited by the molecular oxygen diffusion to the reaction sites, or by the rate of the following oxygen reduction reaction. For the diffusion process, approximate Crank models for
405 both short and long times, and Bangham models were considered, whereas for the adsorption process, according to the literature, pseudo second order (suggested in literature for this reaction [63]), pseudo first and n-th order, Elovich, and Langmuir models [59] were taken into account. The definition equation of all of the models are provided in the Supporting Information, in

ACCEPTED MANUSCRIPT

410 accordance with Ref. [59]. Considering the presence of a single trend, the fit comparison was operated on Gr/SiO_2 and Gr/Al_2O_3 data set only. For both of the samples, the Bangham model – defined as $D = ckt^{\vartheta}$, where k is the rate constant, ϑ is the Bangham parameter, and $c = 10^{13}cm^{-2}$ a scale-constant – resulted the best model to describe the data sets, by showing the 415 lowest value of root mean square of errors (RMSE) (reported in Figure S8), and by operating the F-test bewteen other models whith similar RMSE [59]. On the other hand, in order to describe the progressive doping loss occurring for Gr/HfO_2, its kinetics is evaluated with an extended version of Bangham model, which includes a linear contribution $D = cst$. Moreover, due to the 420 exiguous resolution of doping increase, the ϑ parameter obtained for Gr/SiO_2 was imposed for Gr/HfO_2 fit. The obtained parameters are reported in the following Tab.1.

Sample	k (min^{-1})	ϑ	s (min^{-1})
Gr/SiO_2	0.72(3)	0.13(1)	–
Gr/Al_2O_3	0.36(5)	0.27(3)	–
Gr/HfO_2	0.67(3)	0.13(1)	-0.004(6)

Table 1: Fit parameters obtained for the kinetics analysis. Bangham model, defined as $D = ckt^{\vartheta}$, where k is the rate constant, ϑ is the Bangham parameter, and $c = 10^{13}cm^{-2}$ is the scale-constant, was used for Gr/SiO_2, and Gr/Al_2O_3, whereas for Gr/HfO_2, an additional loss term $D = cst$ was included, and the ϑ parameter obtained for Gr/SiO_2 was imposed.

Therefore, the time scale of doping observed in our experiments is determined by diffusion process by molecular oxygen between Gr and substrate. 425 This finding, in accordance with those studies which relate molecular doping process of supported Gr to diffusion process in the interstitial space between

ACCEPTED MANUSCRIPT

Gr and substrate [36, 64, 65]. Thus, once the reaction sites are reached, it follows a fast reaction whose rate is evaluated in the time-scale of μs–ms by other investigations [66, 67]. Even if the different rates obtained indicate the close relation between the diffusion process and the substrate used, the current data are insufficient to establish a correlation with some specific feature of this latter.

4. Conclusions

In summary, structural and electronic differences between native Gr/SiO_2, Gr/Al_2O_3, and Gr/HfO_2 were found by the correlation of their Raman spectroscopic features. In particular, native samples have different structural strain (Figure 2) related to the more or less rough substrate surface (Figure 3). Moreover, for Gr/HfO_2, a significative fraction of the Gr is folded, and exhibits a reduction of Fermi velocity and inability to doping. By thermal treamtent in O_2 atmosphere, both Gr/Al_2O_3, and Gr/HfO_2-N samples show a strong change in structural and electronic properties of graphene and, in particular, the occurrence of hole doping, similar to the case of Gr/SiO_2. The overall evolution of strain spread and Γ_{2D} suggest an evolution of the graphene structure during the doping process. Distinctive features of the process are found for the various samples: a different highest doping available (Figure 7), a different distribution on temperature of the reactive sites of substrate (Figure 8), and a variation in the reaction rates (Figure 12), thus attesting the close dependence of O_2 doping on the surface properties of the used substrate. The oxygen diffusion between Gr and substrate is found to be the process which limits the kinetics of doping, and which is followed by a faster adsorption process. Finally, we propose a subdivision of the studied samples based on the above discussion. Gr/HfO_2 differs *quan-*

titatively from the other samples for a lower doping, as a consequence of a lower density of reaction sites and water affinity. Nevertheless, as shown in Figure 13, Gr/SiO_2 and Gr/HfO_2 can be *qualitatively* distinguished from Gr/Al_2O_3 by considering both their lower threshold temperature (Figure 8), and their higher reaction rate (Tab.1), suggesting similar surface properties. Therefore, it is supposed that Gr/Al_2O_3 has different surface features, which lead to a highest doping well comparable to Gr/SiO_2, but through a peculiar behavior.

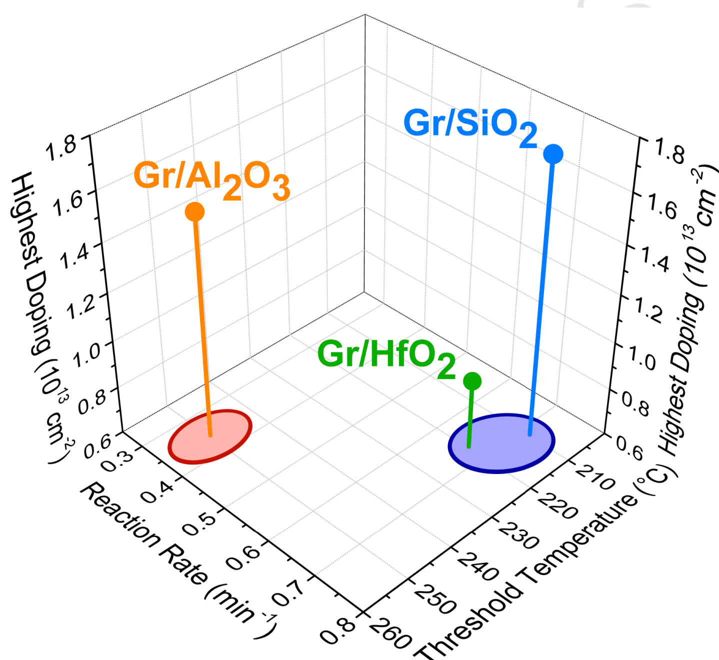

Figure 13: Mean values of highest doping available, reaction rate, and threshold temperature for Gr/SiO_2 (azure), Gr/Al_2O_3 (orange), and **(c)** Gr/HfO_2 (green). The proposed grouping is reported by red and blue ellipses.

Acknowledgements

The authors would like to thank people of the LaBAM group (`http://www.unipa.it/lamp/`) at the Dipartimento di Fisica e Chimica of Università

degli Studi di Palermo, for useful discussions and comments. S. Lo Verso is acknowledged for the contact angle measurement. G. Tricomi and G. Napoli are acknowledged for the assistance during the thermal treatments in controlled atmosphere.

References

[1] A. K. Geim, K. S. Novoselov, The rise of graphene, Nat. Mater. 6 (3) (2007) 183–191.

[2] E. P. Randviir, D. A. Brownson, C. E. Banks, A decade of graphene research: production, applications and outlook, Mater. Today 17 (9) (2014) 426–432.

[3] M. J. Allen, V. C. Tung, R. B. Kaner, Honeycomb carbon: a review of graphene, Chem. Rev. 110 (1) (2009) 132–145.

[4] Y.-M. Lin, C. Dimitrakopoulos, K. Jenkins, D. Farmer, H.-Y. Chiu, A. Grill, P. Avouris, 100-ghz transistors from wafer-scale epitaxial graphene, Science.

[5] C. Mattevi, H. Kim, M. Chhowalla, A review of chemical vapour deposition of graphene on copper, Nat. Nanotechnol. 21 (10) (2011) 3324–3334.

[6] S. Bae, H. Kim, Y. Lee, X. Xu, J.-S. Park, Y. Zheng, , et al., Roll-to-roll production of 30-inch graphene films for transparent electrodes, J. Mater. Chem. 5 (8) (2010) 574–578.

[7] F. Giannazzo, G. Greco, F. Roccaforte, S. Sonde, Vertical transistors based on 2d materials: status and prospects, Crystals 8 (2) (2018) 70.

[8] F. Giannazzo, G. Fisichella, G. Greco, A. La Magna, F. Roccaforte, B. Pécz, et al., Graphene integration with nitride semiconductors for high power and high frequency electronics, Phys. Status Solidi (A) 214 (4).

490 [9] A. Zubair, A. Nourbakhsh, J.-Y. Hong, M. Qi, Y. Song, D. Jena, et al., Hot electron transistor with van der waals base-collector heterojunction and high-performance gan emitter, Nano Lett. 17 (5) (2017) 3089–3096.

[10] C. Mannequin, A. Delamoreanu, L. Latu-Romain, V. Jousseaume, H. Grampeix, S. David, C. Rabot, A. Zenasni, C. Vallee, P. Gonon, 495 Graphene-hfo2-based resistive ram memories, Microelectron. Eng. 161 (2016) 82–86.

[11] S.-B. Kim, J.-Y. Park, C.-S. Kim, K. Okuyama, S.-E. Lee, H.-D. Jang, T.-O. Kim, Effects of graphene in dye-sensitized solar cells based on nitrogen-doped TiO_2 composite, The Journal of Physical Chemistry C 500 119 (29) (2015) 16552–16559.

[12] A. Raja, A. Montoya-Castillo, J. Zultak, X.-X. Zhang, Z. Ye, C. Roquelet, D. A. Chenet, A. M. van der Zande, P. Huang, S. Jockusch, et al., Energy transfer from quantum dots to graphene and MoS_2: The role of absorption and screening in two-dimensional materials, Nano 505 Lett. 16 (4) (2016) 2328–2333.

[13] H. Chang, H. Wu, Graphene-based nanocomposites: preparation, functionalization, and energy and environmental applications, Energy & Environmental Science 6 (12) (2013) 3483–3507.

[14] A. Armano, G. Buscarino, F. Messina, A. Sciortino, M. Cannas, 510 F. Gelardi, F. Giannazzo, E. Schilirò, S. Agnello, Photoinduced charge

transfer from carbon dots to graphene in solid composite, Thin Solid Films.

[15] F. Schwierz, Graphene transistors, Nat. Nanotechnol. 5 (7) (2010) 487–496.

515 [16] K. Patel, P. K. Tyagi, P-type multilayer graphene as a highly efficient transparent conducting electrode in silicon heterojunction solar cells, Carbon 116 (2017) 744–752.

[17] F. Bonaccorso, Z. Sun, T. Hasan, A. Ferrari, Graphene photonics and optoelectronics, Nat. Photonics 4 (9) (2010) 611–622.

520 [18] S.-J. Jeong, Y. Gu, J. Heo, J. Yang, C.-S. Lee, M.-H. Lee, Y. Lee, H. Kim, S. Park, S. Hwang, Thickness scaling of atomic-layer-deposited hfo 2 films and their application to wafer-scale graphene tunnelling transistors, Sci. Rep. 6 (2016) 20907.

[19] M. A. Rehman, I. Akhtar, W. Choi, K. Akbar, A. Farooq, S. Hussain,
525 M. A. Shehzad, S.-H. Chun, J. Jung, Y. Seo, Influence of an al2o3 interlayer in a directly grown graphene-silicon schottky junction solar cell, Carbon 132 (2018) 157–164.

[20] S.-Y. Kim, Y. J. Kim, U. Jung, B. H. Lee, Chemically induced fermi level pinning effects of high-k dielectrics on graphene, Sci. Rep. 8 (1)
530 (2018) 2992.

[21] D. Misra, H. Iwai, H. Wong, High-k gate dielectrics, Interface 14 (2) (2005) 30–34.

[22] G. Bersuker, P. Zeitzoff, G. Brown, H. Huff, Dielectrics for future transistors, Mater. Today 7 (1) (2004) 26–33.

ACCEPTED MANUSCRIPT

535 [23] J. Kittl, K. Opsomer, M. Popovici, N. Menou, B. Kaczer, X. Wang, C. Adelmann, M. Pawlak, K. Tomida, A. Rothschild, et al., High-k dielectrics for future generation memory devices, Microelectron. Eng. 86 (7-9) (2009) 1789–1795.

[24] C. Zhao, C. Z. Zhao, S. Taylor, P. R. Chalker, Review on non-volatile
540 memory with high-k dielectrics: flash for generation beyond 32 nm, Materials 7 (7) (2014) 5117–5145.

[25] L. D'Arsié, S. Esconjauregui, R. S. Weatherup, X. Wu, W. E. Arter, H. Sugime, et al., Stable, efficient p-type doping of graphene by nitric acid, RSC Adv. 6 (114) (2016) 113185–113192.

545 [26] S. Ryu, L. Liu, S. Berciaud, Y.-J. Yu, H. Liu, P. Kim, et al., Atmospheric oxygen binding and hole doping in deformed graphene on a sio2 substrate, Nano Lett. 10 (12) (2010) 4944–4951.

[27] A. Tiberj, M. Rubio-Roy, M. Paillet, J.-R. Huntzinger, P. Landois, M. Mikolasek, et al., Reversible optical doping of graphene, Sci. Rep. 3
550 (2013) 2355.

[28] S. Costa, J. E. Weis, O. Frank, M. Fridrichová, M. Kalbac, Monitoring the doping of graphene on sio 2/si substrates during the thermal annealing process, RSC Adv. 6 (76) (2016) 72859–72864.

[29] A. Piazza, F. Giannazzo, G. Buscarino, G. Fisichella, A. L. Magna,
555 Roccaforte, et al., Graphene p-type doping and stability by thermal treatments in molecular oxygen controlled atmosphere, J. Phys. Chem. C 119 (39) (2015) 22718–22723. doi:10.1021/acs.jpcc.5b07301. URL http://dx.doi.org/10.1021/acs.jpcc.5b07301

[30] J. H. Lee, A. Avsar, J. Jung, J. Y. Tan, K. Watanabe, T. Taniguchi,
560 et al., Van der waals force: a dominant factor for reactivity of graphene, Nano Lett. 15 (1) (2014) 319–325.

[31] F. Schedin, A. K. Geim, S. V. Morozov, E. Hill, P. Blake, M. Katsnelson, K. Novoselov, Detection of individual gas molecules adsorbed on graphene, Nat. Mater. 6 (9) (2007) 652–655.

565 [32] F. R. Bagsican, A. Winchester, S. Ghosh, X. Zhang, L. Ma, M. Wang, H. Murakami, et al., Adsorption energy of oxygen molecules on graphene and two-dimensional tungsten disulfide, Sci. Rep. 7.

[33] H. Xu, Y. Chen, J. Zhang, H. Zhang, Investigating the mechanism of hysteresis effect in graphene electrical field device fabricated on sio2
570 substrates using raman spectroscopy, Small 8 (18) (2012) 2833–2840.

[34] P. L. Levesque, S. S. Sabri, C. M. Aguirre, J. Guillemette, M. Siaj, P. Desjardins, et al., Probing charge transfer at surfaces using graphene transistors, Nano Lett. 11 (1) (2010) 132–137.

[35] L. Zheng, X. Cheng, Z. Wang, C. Xia, D. Cao, L. Shen, et al., Reversible
575 n-type doping of graphene by h2o-based atomic-layer deposition and its doping mechanism, J. Phys. Chem. C 119 (11) (2015) 5995–6000.

[36] D. Lee, G. Ahn, S. Ryu, Two-dimensional water diffusion at a graphene–silica interface, J. Am. Chem. Soc. 136 (18) (2014) 6634–6642.

[37] Q. H. Wang, Z. Jin, K. K. Kim, A. J. Hilmer, G. L. Paulus, C.-J. Shih,
580 M.-H. Ham, J. D. Sanchez-Yamagishi, K. Watanabe, T. Taniguchi, et al., Understanding and controlling the substrate effect on graphene electron-transfer chemistry via reactivity imprint lithography, Nat. Chem. 4 (9) (2012) 724.

ACCEPTED MANUSCRIPT

[38] A. Armano, G. Buscarino, M. Cannas, F. Gelardi, F. Giannazzo, E. Schilirò, S. Agnello, Monolayer graphene doping and strain dynamics induced by thermal treatments in controlled atmosphere, Carbon 127 (2018) 270–279.

[39] A. Piazza, F. Giannazzo, G. Buscarino, G. Fisichella, A. L. Magna, F. Roccaforte, et al., Substrate and atmosphere influence on oxygen p-doped graphene, Carbon 107 (2016) 696–704. doi:http://doi.org/10.1016/j.carbon.2016.06.077.
URL http://www.sciencedirect.com/science/article/pii/S0008622316305322

[40] A. Piazza, F. Giannazzo, G. Buscarino, G. Fisichella, A. La Magna, F. Roccaforte, M. Cannas, F. M. Gelardi, S. Agnello, Effect of air on oxygen p-doped graphene on sio2, Phys. Status Solidi (A) 213 (9) (2016) 2341–2344.

[41] J. H. Parker, D. W. Feldman, M. Ashkin, Raman scattering by silicon and germanium, Phys. Rev. 155 (1967) 712–714. doi:10.1103/PhysRev.155.712.
URL https://link.aps.org/doi/10.1103/PhysRev.155.712

[42] P. A. Temple, C. E. Hathaway, Multiphonon raman spectrum of silicon, Phys. Rev. B 7 (1973) 3685–3697. doi:10.1103/PhysRevB.7.3685.
URL https://link.aps.org/doi/10.1103/PhysRevB.7.3685

[43] D. Yoon, H. Moon, Y.-W. Son, J. S. Choi, B. H. Park, Y. H. Cha, Y. D. Kim, H. Cheong, Interference effect on raman spectrum of graphene on sio 2/si, Phys. Rev. B 80 (12) (2009) 125422.

[44] A. C. Ferrari, D. M. Basko, Raman spectroscopy as a versatile tool for studying the properties of graphene, Nature nanotechnology 8 (4) (2013)
610 235.

[45] J. E. Lee, G. Ahn, J. Shim, Y. S. Lee, S. Ryu, Optical separation of mechanical strain from charge doping in graphene, Nat. Commun. 3 (2012) 1024.

[46] T. G. A. Verhagen, K. Drogowska, M. Kalbac, J. Vejpravova,
615 Temperature-induced strain and doping in monolayer and bilayer isotopically labeled graphene, Phys. Rev. B 92 (12) (2015) 125437.

[47] C. Metzger, S. Rémi, M. Liu, S. V. Kusminskiy, A. H. Castro Neto, A. K. Swan, et al., Biaxial strain in graphene adhered to shallow depressions, Nano Lett. 10 (1) (2009) 6–10.

620 [48] C. Thomsen, S. Reich, P. Ordejon, Ab initio determination of the phonon deformation potentials of graphene, Phys. Rev. B 65 (7) (2002) 073403.

[49] T. M. G. Mohiuddin, A. Lombardo, R. R. Nair, A. Bonetti, G. Savini, R. Jalil, et al., Uniaxial strain in graphene by raman spectroscopy: G peak splitting, grüneisen parameters, and sample orientation, Phys. Rev.
625 B 79 (20) (2009) 205433.

[50] D. Mafra, G. Samsonidze, L. Malard, D. Elias, J. Brant, F. Plentz, E. Alves, M. Pimenta, Determination of la and to phonon dispersion relations of graphene near the dirac point by double resonance raman scattering, Phys. Rev. B 76 (23) (2007) 233407.

630 [51] R. Zhou, S. Yasuda, H. Minamimoto, K. Murakoshi, Sensitive raman probe of electronic interactions between monolayer graphene and sub-

ACCEPTED MANUSCRIPT

strate under electrochemical potential control, ACS Omega 3 (2) (2018) 2322–2328.

[52] C. Hwang, D. A. Siegel, S.-K. Mo, W. Regan, A. Ismach, Y. Zhang,
635 A. Zettl, A. Lanzara, Fermi velocity engineering in graphene by substrate modification, Sci. Rep. 2 (2012) 590.

[53] Z. Ni, Y. Wang, T. Yu, Y. You, Z. Shen, Reduction of fermi velocity in folded graphene observed by resonance raman spectroscopy, Phys. Rev. B 77 (23) (2008) 235403.

640 [54] G. Ahn, H. R. Kim, T. Y. Ko, K. Choi, K. Watanabe, T. Taniguchi, B. H. Hong, S. Ryu, Optical probing of the electronic interaction between graphene and hexagonal boron nitride, ACS nano 7 (2) (2013) 1533–1541.

[55] M. L. Hair, Hydroxyl groups on silica surface, J. Non-Cryst. Solids 19
645 (1975) 299–309.

[56] L. Zhuravlev, The surface chemistry of amorphous silica. zhuravlev model, Colloids Surf., A 173 (1-3) (2000) 1–38.

[57] J. Yang, E. Wang, Reaction of water on silica surfaces, Curr. Opin. Solid State Mater. Sci. 10 (1) (2006) 33–39.

650 [58] A. M. Schrader, J. I. Monroe, R. Sheil, H. A. Dobbs, T. J. Keller, Y. Li, S. Jain, M. S. Shell, J. N. Israelachvili, S. Han, Surface chemical heterogeneity modulates silica surface hydration, Proceedings of the National Academy of Sciences 115 (12) (2018) 2890–2895.

[59] L. Largitte, R. Pasquier, A review of the kinetics adsorption models

ACCEPTED MANUSCRIPT

655 and their application to the adsorption of lead by an activated carbon, Chem. Eng. Res. Des. 109 (2016) 495–504.

[60] C. P. Bergmann, F. M. Machado, Carbon nanomaterials as adsorbents for environmental and biological applications, Springer, 2015.

[61] V. Mishra, Modeling of batch sorber system: kinetic, mechanistic, and 660 thermodynamic modeling, Applied Water Science 7 (6) (2017) 3173–3180.

[62] W. Plazinski, W. Rudzinski, A. Plazinska, Theoretical models of sorption kinetics including a surface reaction mechanism: a review, Adv. Colloid Interface Sci. 152 (1-2) (2009) 2–13.

665 [63] D. L. Baulch, D. Drysdale, D. G. Horne, A. C. Lloyd, Evaluated Kinetic Data for High Temperature Reactions, Volume 1: Homogeneous Gas Phase Reactions of the H2-O2-System, Butter-worths & Co., 1972.

[64] T. O. Wehling, A. I. Lichtenstein, M. I. Katsnelson, First-principles studies of water adsorption on graphene: The role of the substrate, 670 Appl. Phys. Lett. 93 (20) (2008) 202110.

[65] R. Larciprete, S. Ulstrup, P. Lacovig, M. Dalmiglio, M. Bianchi, F. Mazzola, L. Hornekær, F. Orlando, A. Baraldi, P. Hofmann, et al., Oxygen switching of the epitaxial graphene–metal interaction, ACS Nano 6 (11) (2012) 9551–9558.

675 [66] Y. G. Lee, C. G. Kang, U. J. Jung, J. J. Kim, H. J. Hwang, H.-J. Chung, S. Seo, R. Choi, B. H. Lee, Fast transient charging at the graphene/sio 2 interface causing hysteretic device characteristics, Appl. Phys. Lett. 98 (18) (2011) 183508.

ACCEPTED MANUSCRIPT

[67] Y. G. Lee, C. G. Kang, C. Cho, Y. Kim, H. J. Hwang, B. H. Lee,
680 Quantitative analysis of hysteretic reactions at the interface of graphene and sio2 using the short pulse i–v method, Carbon 60 (2013) 453–460.

ACCEPTED MANUSCRIPT